Plasmon-Driven Oxidative Coupling of Aniline-Derivative Adsorbates: A Comparative Study of *para*-Ethynylaniline and *para*-Mercaptoaniline

Kexun Chen (陳克迅) and Hui Wang (王輝)*

Department of Chemistry and Biochemistry, University of South Carolina, Columbia, South Carolina 29208, United States

Email: wang344@mailbox.sc.edu; Phone: 1-803-777-2203; orcid.org/0000-0002-1874-5137.

^{*} To whom correspondence should be addressed.

ABSTRACT

Plasmon-driven photocatalysis has emerged as a paradigm-shifting approach, based upon which the energy of photons can be judiciously harnessed to trigger interfacial molecular transformations on metallic nanostructure surfaces in a regioselective manner with nanoscale precision. Over the past decade, the formation of aromatic azo compounds through plasmon-driven oxidative coupling of thiolated aniline-derivative adsorbates has become a testbed for developing detailed mechanistic understanding of plasmon-mediated photochemistry. Such photocatalytic bimolecular coupling reactions may occur not only between thiolated aniline-derivative adsorbates but between their nonthiolated analogues as well. How the nonthiolated adsorbates behave differently from their thiolated counterparts during the plasmon-driven coupling reactions, however, remains largely unexplored. Here, we systematically compare an alkynylated aniline-derivative, paraethynylaniline, to its thiolated counterpart, para-mercaptoaniline, in terms of their adsorption conformations, structural flexibility, photochemical reactivity, and transforming kinetics on Ag nanophotocatalyst surfaces. We employ surface-enhanced Raman scattering as an in situ spectroscopic tool to track the detailed structural evolution of the transforming molecular adsorbates in real time during the plasmon-driven coupling reactions. Rigorous analysis of the spectroscopic results, further aided by density functional theory calculations, lays an insightful knowledge foundation that enables us to elucidate how the alteration of the chemical nature of metal-adsorbate interactions profoundly influences the transforming behaviors of the molecular adsorbates during plasmon-driven photocatalytic reactions.

INTRODUCTION

Relaxation of optically excited free electron oscillations in metallic nanostructures, known as localized plasmons, gives rise to a series of intriguing photophysical effects, such as nonthermal distribution of hot charge carriers, local field enhancements, and photothermal transduction, all of which can be deliberately harnessed to catalyze interfacial photochemical processes, including both bond-cleaving molecular scissoring and bond-forming coupling reactions. 1-12 Photocatalytic molecular transformations on nanostructured metal surfaces may occur through several distinct plasmon-mediated reaction pathways involving plasmon-enhanced intramolecular electronic excitations, 13-16 hot carrier injection into the molecular adsorbates, 17-21 or photothermal activation of certain chemical bonds.²²⁻²⁴ In numerous cases, the kinetic profiles associated with plasmonmediated surface photochemistry are intimately tied to the strong interplay among hot carriers, field enhancements, and photothermal heating rather than being dictated solely by one specific plasmon-derived effect.^{7,25-31} Besides their photocatalytic functions, metallic nanostructures can also serve as substrates for plasmon-enhanced Raman spectroscopies, such as surface-enhanced Raman scattering (SERS) and tip-enhanced Raman scattering (TERS).³²⁻³⁸ Because the hot spots for Raman signal enhancement spatially coincide with the active sites for photocatalysis on the nanostructure surfaces, plasmon-enhanced Raman spectroscopies can be utilized as a unique in situ spectroscopic tool with molecular fingerprinting capability to fine-resolve the detailed structural evolution of the transforming molecular adsorbates, 25,39-43 a key step toward thorough understanding of the plasmon-mediated reaction mechanisms.

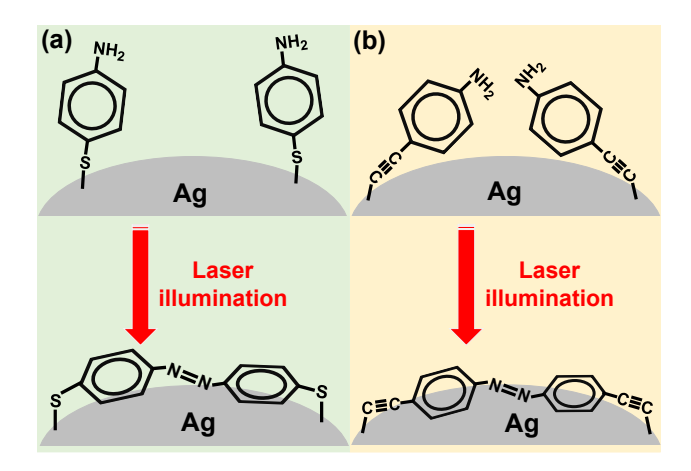
Plasmon-driven oxidative coupling of aniline-derivatives represents a paradigm-shifting approach to the synthesis of aromatic azo compounds. The discovery and mechanistic studies of this type of reactions trace back to the 1990s when Osawa and coworkers⁴⁴ first observed three

unexpected peaks at 1438, 1388, and 1140 cm⁻¹ in the SERS spectra of para-mercaptoaniline (pMA) chemisorbed to roughened Ag surfaces, whereas none of these peaks were observable in the normal Raman (NR) spectra of pMA. The origin of these anomalous SERS peaks had been under intense debate⁴⁵⁻⁵¹ until 2010 when Tian and coworkers⁵² convincingly proved that surfaceadsorbed pMA underwent a bimolecular coupling reaction to produce p,p'-dimercaptoazobenzene (DMAB) under laser illumination during the SERS measurements. Over the past decade, this reaction has become a testbed for developing detailed understanding of the complex reaction mechanisms underpinning plasmon-driven photocatalysis. The rates and yields of the pMA coupling reactions vary significantly from case to case, depending on the plasmonic characteristics of the photocatalysts, the optical excitation conditions, and the local environments in which the reactions occur. 47,49,53-56 Despite the seemingly divergent kinetic results reported in the literature, a unified mechanistic picture has started to emerge, built upon the mechanistic insights gained from deliberately designed SERS/TERS measurements. Under anaerobic reaction conditions, the plasmonic hot holes serve as the primary driving force for the oxidative coupling of pMA, and the reactions can be kinetically boosted with the aid of electron acceptors, which effectively promote the charge carrier separation.^{57,58} In aerobic reaction environments, however, this oxidative coupling reaction switches to a more efficient, hot electron-driven pathway, in which the plasmonic hot electrons are injected into the antibonding orbitals of surface-adsorbed O₂, leading to the formation of highly reactive anionic O_2 radicals that are capable of oxidizing pMA.^{56,59} When the photoactivated O_2^- reaches the steady state coverage on the photocatalyst surfaces, this reaction obeys the first-order rate law, suggesting that the rate-limiting step is the oxidation of pMA by O₂⁻ rather than the photoactivation of O₂ or the azo bond formation.⁶⁰ The dimerization process imposes certain geometric requirements on the molecular adsorbates regarding their

surface orientations and structural flexibility. As revealed by recent TERS studies, structurally flexible *p*MA molecules on ill-defined Ag nanoparticle (NP) surfaces rapidly couple into DMAB, whereas a structurally ordered *p*MA monolayer on a well-defined Ag {111} surface remains unreactive under identical photoexcitation conditions.⁶¹ In plasmon-driven dimerization of *para*-nitrothiophenol (*p*NTP), which is the reductive analog of the *p*MA coupling reaction, the reactivity has also been observed to be closely related to the surface orientation and structural flexibility of *p*NTP adsorbates.^{62,63} These observations strongly suggest that we should take not only the plasmonic effects but also the adsorbate structures into careful consideration when designing metal-adsorbate systems for plasmon-driven photocatalysis.

While organothiols constitute so far the most intensively studied molecular adsorbate system, molecules can also use a variety of alternative chemical moieties, such as diazonium, $^{64-71}$ isocyanide, $^{72-77}$ N-heterocyclic carbene, $^{78-83}$ and alkyne, $^{84-87}$ as the anchoring groups to form covalent interactions with metal surfaces. The plasmon-mediated bimolecular coupling reactions are not restricted to thiolated aniline-derivatives only, but may occur between nonthiolated aniline-derivatives as well. 88 However, it remains unclear how the nonthiolated aniline-derivatives behave differently from their thiolated counterparts due to lack of rigorous comparative studies in the literature. In this work, we systematically compare the plasmon-driven transforming behaviors of an alkynylated aniline-derivative, *para*-ethynylaniline (*p*EA), to those of the benchmarking thiolated aniline-derivative, *pMA*. Analogous to *pMA*, *pEA* may also undergo plasmon-driven oxidative coupling reactions to form an azo compound, *p.p'*-diynylazobenzene (DYAB), on Ag NP surfaces, as illustrated in Scheme 1. While the Ag-thiol interactions lead to the formation of Ag-S bonds through σ electron donation, the interactions between Ag and an ethynyl group involve both σ -donation and π -back donation, forcing the alkynylated adsorbates to adopt adsorption

conformations remarkably different from those of their thiolated counterparts. 85,86 The difference in bonding nature may also result in very different local structural flexibility when the molecules are chemisorbed to metal surfaces. Therefore, pEA and pMA represent two contrasting types of aniline-derivatives that are well-worthy of detailed comparative studies. Here we used SERS as an in situ spectroscopic tool, with the aid of density functional theory (DFT) calculations, to correlate the kinetic characteristics of the plasmon-driven coupling reactions to the detailed structures of the transforming adsorbates on Ag NP surfaces. Insights gained from our systematic comparative studies shed light on the crucial roles of the metal-adsorbate interactions in determining the adsorbate conformations molecule-transforming kinetics during and plasmon-driven photocatalytic reactions.



Scheme 1. Schematic illustration of plasmon-driven oxidative coupling of (a) pMA and (b) pEA chemisorbed on Ag NP surfaces.

RESULTS AND DISCUSSION

We used Ag NPs as the building blocks to assemble close-packed NP array structures, which played a dual role as both the substrates for SERS and the plasmonic photocatalysts for the coupling reactions. Colloidal Ag NPs were synthesized through seed-mediated nanocrystal growth using cetyltrimethylammonium chloride (CTAC) as the surface-capping molecular ligands. The

as-synthesized Ag NPs exhibited a uniform quasi-spherical morphology (Figure 1a) with diameters of 45 ± 4.2 nm (Figure 1b). The colloidal Ag NPs displayed a well-defined plasmon resonance peak centered at ~412 nm, which matched the results calculated by the Mie scattering theory in terms of both resonance wavelengths and spectral lineshapes (Figure 1c). The CTAC ligands on the surfaces of the as-synthesized Ag NPs could be readily displaced by pEA and pMA, both of which were bound to Ag surfaces more strongly than CTAC. The Ag NPs were further assembled into close-packed array structures with a high density of sub-10 nm interparticle gaps (Figure 1d and Figure S1 in Supplementary Information) through slow solvent evaporation of aqueous colloidal inks containing CTAC-, pEA-, or pMA-coated Ag NPs on indium tin oxide (ITO)-coated glass substrates. The strong plasmon coupling among neighboring Ag NPs led to the emergence of a broad plasmon resonance band across the visible and near-infrared spectral regions (Figure 1e). Upon resonant excitations of the plasmons in the Ag NP arrays using a continuous wave (cw) near-infrared laser (785 nm), the local electric fields were enormously enhanced in the interparticle gaps, creating electromagnetic hot spots for not only SERS but plasmon-driven photocatalysis as well. To ensure that the CTAC ligands were completely displaced by pEA or pMA, we incubated the as-synthesized colloidal Ag NPs with 1.0 mM of pEA or pMA for 2 h. The pEA- and pMAcoated colloidal Ag NPs were then centrifuged and redispersed in water before eventually selfassembled into the array structures for SERS measurements. To fully resolve the spectral features of pEA and pMA adsorbates without the interference by any photochemical reactions, the SERS spectra were collected at a low laser excitation power (P_{ex}) of 0.5 mM with a spectral acquisition time of 1 s while the SERS substrates were exposed to an aqueous solution of 100 mM ammonia borane, a reducing agent that effectively prohibited the oxidative coupling of the aniline derivatives. After ligand exchange, all the SERS spectral features of CTAC vanished, while the

characteristic peaks of pEA or pMA, such as the benzene ring breathing ($v_{CC ring}$), C=C stretching ($v_{C=C}$), C-S stretching (v_{CS}), and C-H in-plane scissoring (β_{C-H}) modes, emerged in the SERS spectra (Figure S2 in Supplementary Information). In particular, the disappearance of the strong Ag-Cl vibrational peak (v_{AgCl}) at ~190 cm⁻¹, together with the emergence of the characteristic v_{AgC} (440 cm⁻¹) and v_{AgS} (390 cm⁻¹) modes, verified that CTAC was fully exchanged with pEA and pMA, which were chemisorbed to the Ag NP surfaces through Ag-C and Ag-S bonds, respectively.

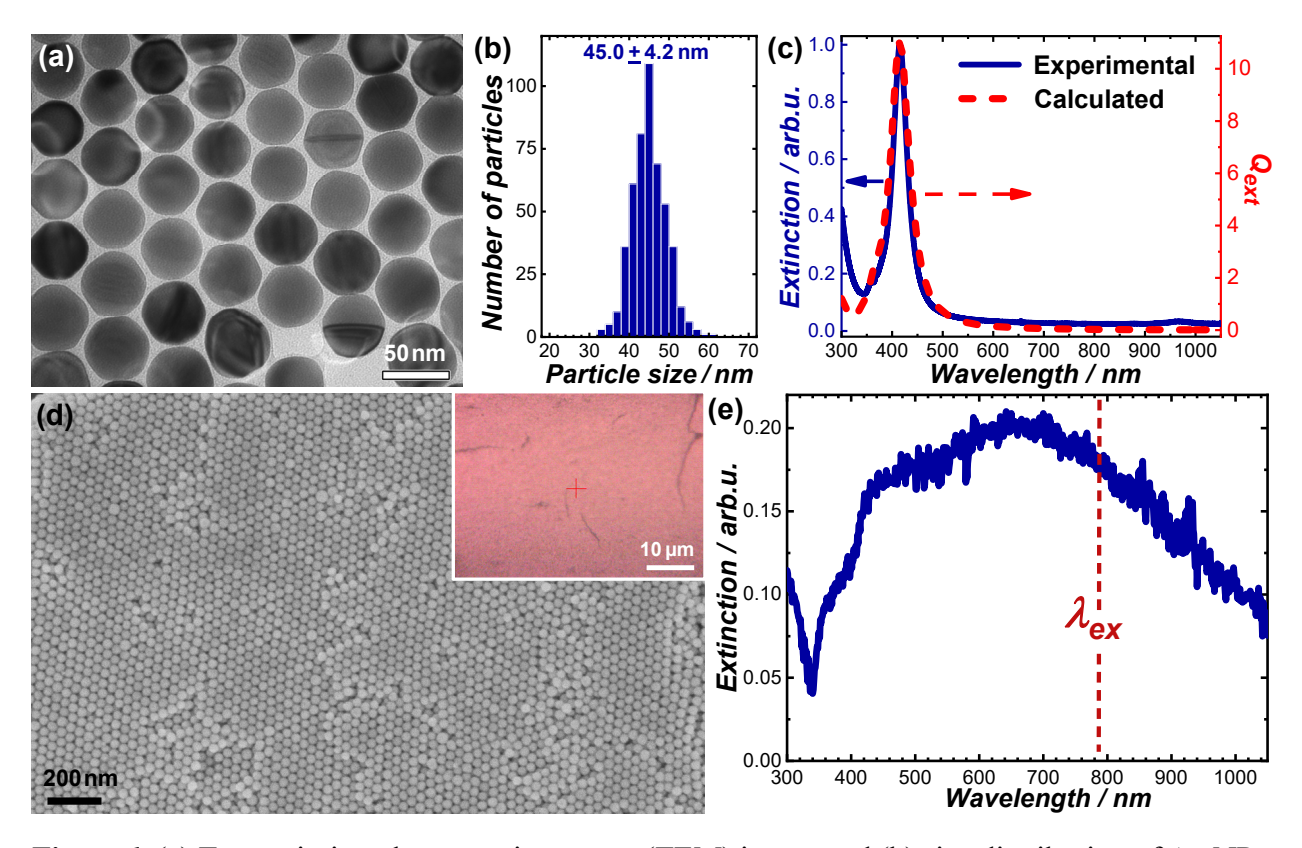


Figure 1. (a) Transmission electron microscopy (TEM) image and (b) size distribution of Ag NPs. (c) Experimentally measured extinction spectrum of colloidal Ag NPs dispersed in water (solid navy curve) and calculated wavelength-dependent extinction efficiencies, Q_{ext} , of an Ag nanosphere (45 nm in diameter) in a homogenous dielectric medium with a refractive index of 1.33 (dash red curve). (d) Scanning electron microscopy (SEM) image of *p*EA-coated Ag NP arrays self-assembled on an ITO-coated glass slide, which served as both the SERS substrate and the plasmonic photocatalyst in this work. The inset shows a dark-field optical microscopy image of the Ag NP arrays. (e) Extinction spectrum of the Ag NP arrays immersed in water. The wavelength of the excitation laser (λ_{ex}) used for the plasmon-driven reactions and SERS measurements is labeled with a vertical dash line.

Careful comparison of the NR and SERS spectral features, in combination with DFT calculations, enabled us to gain detailed insights into the chemical nature of the metal-adsorbate interactions. The NR spectrum collected from a solid film of pEA was dominated by three vibrational peaks corresponding to the $v_{C=C}$, $v_{CC ring}$, and β_{CH} modes, respectively, all of which were also clearly observed in the SERS spectrum of pEA on the Ag NP surfaces (Figure 2a). Although the $v_{CC ring}$ and β_{CH} modes both exhibited similar Raman shifts in the NR and SERS spectra, the v_{C=C} mode at 2095 cm⁻¹ in the NR spectrum down-shifted to 1945 cm⁻¹ in the SERS spectrum, indicating that the chemisorption of pEA to Ag resulted in significant weakening of the C \equiv C bond in the ethynyl group. We also used DFT to calculate the Raman spectra of pEA and a pEA molecule covalently linked to an Ag₁₄ atomic cluster (represented as a unit cell of face-centered cubic crystalline lattice). When calculating the NR spectrum of pEA, we only included a single pEA molecule without considering the intermolecular interactions possibly existing in the solid-state samples, which might give rise to some minor differences between the calculated and measured NR spectral features. For example, in the DFT-calculated NR spectrum of pEA (Figure 2a), two Raman peaks with comparable intensities were observed at 1158 and 1193 cm⁻¹, which were associated with the asymmetric and symmetric β_{CH} modes, respectively. Both peaks were slightly upshifted in the experimentally measured NR spectrum of pEA, and the symmetric β_{CH} mode became significantly weaker than the asymmetric β_{CH} mode. Although DFT was incapable of accurately predicting the relative peak intensities in the SERS spectra because it calculated the NR spectrum of the pEA-Ag₁₄ compound rather than the SERS of pEA on a metal surface, the Raman shifts of all the major peaks calculated by DFT were in very good agreement with those in the experimentally measured SERS spectrum (Figure 2a). The significant spectral downshift of the $v_{C=C}$ mode by ~ 150 cm⁻¹, which was both experimentally observed and computationally verified,

signified the hybrid $\sigma\pi$ bonding nature of the Ag-ethynyl interactions. The σ component arose from the overlap of a filled π orbital of the alkyne with the conduction band of Ag, while the π component was caused by the overlap of an unoccupied π^* orbital of the alkyne with valence band of Ag. 86 The hybrid $\sigma\pi$ bonding required the ethynyl group of pEA to be significantly tilted toward the Ag surface, as shown in the DFT-optimized conformation of pEA-Ag₁₄, denoted as pEA-Ag₁₄o (Figure 2b). When the pEA molecule chemisorbed to Ag₁₄ through a atop conformation with the C \equiv C bond aligned vertically to the Ag surface (denoted as pEA-Ag₁₄-v), the Ag-ethynyl interaction was dominated by σ donation without the contribution of π -back donation. The DFT results showed that the $v_{C=C}$ mode of the pEA-Ag₁₄-v conformation had a higher vibrational frequency than that of the pEA-Ag₁₄-o conformation, upshifted from 1945 to 2030 cm⁻¹ (Figure S3 in Supplementary Information). The calculated lengths of the C≡C bond decreased in the order of pEA-Ag₁₄-o > pEA-Ag₁₄-v > unbound pEA (Figure S4 in Supporting Information). These results clearly indicated that both the σ -donation and π -back donation contributed to the experimentally observed spectral downshift of the $v_{C=C}$ mode when pEA was chemisorbed to Ag surfaces. In contrast to the $\sigma\pi$ bonding nature of Ag-acetylene interactions, thiolated molecules were chemisorbed to Ag surfaces through σ donation of the lone-pair electrons of S to the conduction band of Ag. The v_{CS} mode of pMA slightly downshifted from 1085 cm⁻¹ in the NR spectrum to 1077 cm⁻¹ in the SERS spectrum (Figure 2c), indicating that the formation of Ag-S bond had rather insignificant influence on the bond length of the C-S bond in pMA, which was further verified by DFT calculations (Figure S4 in Supplementary Information). The DFToptimized geometry of pMA-Ag₁₄ (Figure 2d) revealed that pMA was chemisorbed to Ag₁₄ at a bridge site with a relatively vertical orientation that was only tilted slightly from the normal to the Ag surface, in line with previous DFT calculations.⁶¹ The single-bond nature of the C-S bond

created certain level of motional freedom of the reactive amine-group due to rotation around the surface normal. Therefore, pMA was expected to be structurally more flexible than pEA when chemisorbed to the Ag NP surfaces, especially at the locally curved surface sites. We also used DFT to calculate the binding energies, $\Delta E_{binding}$, of pEA and pMA to an Ag₁₄ atomic cluster, which corresponded to the energy difference between the molecule-cluster complex (pEA-Ag₁₄ or pMA-Ag₁₄) and the unbound species (Ag₁₄ + pEA or pMA). The values of $\Delta E_{binding}$ were calculated to be -87.8 kcal mol⁻¹ for pEA and -58.9 kcal mol⁻¹ for pMA, respectively.

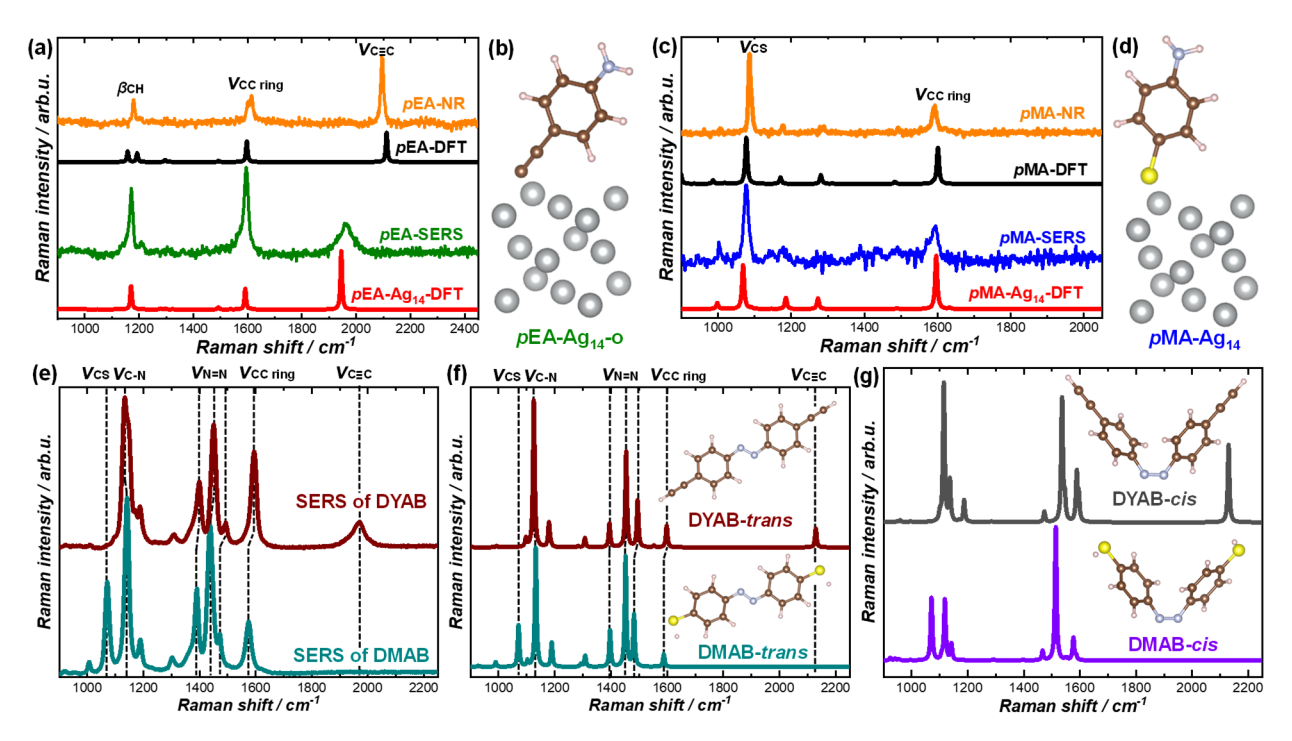


Figure 2. (a) Normal Raman (NR) spectrum of neat pEA and SERS spectrum of pEA chemisorbed on Ag. DFT-calculated Raman spectra of pEA and pEA-Ag₁₄ are also shown for comparison. The characteristic Raman peaks of the $v_{C\equiv C}$, $v_{CC \text{ ring}}$, and $β_{CH}$ modes are labeled. (b) Geometry of pEA-Ag₁₄ optimized by DFT. (c) NR spectrum of neat pMA and SERS spectrum of pMA chemisorbed on Ag. DFT-calculated Raman spectra of pMA and pMA-Ag₁₄ are also shown for comparison. The characteristic Raman peaks of the v_{CS} and $v_{CC \text{ ring}}$ modes are labeled. (d) Geometry of pMA-Ag₁₄ optimized by DFT. (e) SERS spectra of DYAB and DMAB after the pEA-coated and pMA-coated Ag NP substrates were exposed to the excitation laser at a P_{ex} of 5.8 mW for 20 s. Various characteristic vibrational modes are labeled with vertical dash lines. DFT-calculated Raman spectra of DYAB and DMAB in the (f) trans and (g) trans trans and trans trans trans trans and trans tra

The pEA and pMA adsorbates on Ag NP surfaces underwent plasmon-driven oxidative coupling reactions in an alkaline aqueous environment containing dissolved molecular O₂. After continuously illuminated by the 785 nm laser at a P_{ex} of 5.8 mW for 20 s, pEA and pMA dimerized into DYAB and DMAB, respectively, resulting in the emergence of several characteristic SERS peaks of the azo compounds (Figure 2e), including the C-N stretching mode (v_{CN}) around 1140 cm⁻¹ and three peaks in the wavenumber range of 1350-1500 cm⁻¹, all of which were the spectral signatures of the newly formed azo bond ($v_{N=N}$). The DFT results showed that DYAB and DMAB in the *trans* conformation (Figure 2f) had Raman features drastically different from those of their counterparts in the *cis* conformation (Figure 2g). According to our SERS results (Figure 2e), the photochemically produced DYAB and DMAB were both in the thermodynamically favored *trans* conformation rather than the metastable *cis* conformation. All the $v_{N=N}$ modes and the v_{CC} ring modes of DYAB consistently exhibited larger Raman shifts than those of DMAB in the SERS spectra (Figure 2e), which was a spectral feature fully captured by the DFT calculations as well (Figure 2f).

We used SERS as an *in-situ* monitoring tool to track the progress of the pEA coupling reactions in real time. The SERS-based kinetic measurements were conducted using a confocal Raman microscope, which allowed us to focus the 785 nm cw laser onto a focal spot that was 2 μ m in diameter on the samples through a 50× objective (NA=0.5, WD=10.6 mm). The SERS signals were collected in a back scattering configuration using the same objective. The plasmon-driven coupling reactions were carried out in a homebuilt reaction chamber⁸⁹ assembled on top of the ITO-supported Ag NP arrays in an aqueous medium containing 100 mM KOH (pH = 13) at room temperature. It has been previously reported that an alkaline environment favors the plasmon-driven coupling of pMA because pMA-to-DMAB conversion requires dehydrogenation of the

reacting amine groups.⁵⁴ Figure 3a shows the temporal evolution of the SERS spectra collected from a fixed spot on a pEA-coated Ag NP substrate under continuous laser illumination at a $P_{\rm ex}$ of 3.5 mW. Several snapshot SERS spectra captured at various reaction times are shown in Figure 3b. The characteristic v_{CN} and $v_{\text{N=N}}$ peaks of DYAB emerged in the SERS spectra upon initiation of the coupling reaction and became progressively more intense as the reaction further proceeded. The peak intensity of the $v_{CC ring}$ mode also increased over time, because dimerization of pEA into DYAB led to a significant increase in the Raman cross-sections of the molecules. 90 Although the vibrational frequency of $v_{C=C}$ mode was highly sensitive to the surface orientation of the C=C triple bond, neither detectable peak shift nor any resolvable lineshape change of the v_{C≡C} mode was observed in the time-resolved SERS spectra, suggesting that the molecules remained chemisorbed to Ag with minimal orientational changes of the C=C triple bond during the coupling reactions. Under our reaction conditions, only the pEA adsorbates in the hot spots in the interparticle gaps underwent the coupling reactions to form DYAB, while pEA molecules residing in the electromagnetically colder sites outside the hot spots remained unreacted. As schematically illustrated in Figure S5 in Supplementary Information, the coupling reaction may occur either between pEA molecules on the surfaces of two adjacent Ag NPs to form an interparticle DYAB bridging the interparticle gaps or between two pEA molecules on the surface of the same Ag NP to form an intraparticle DYAB. Considering the geometric requirements, it was most likely that the interparticle DYAB molecules were only produced in a tiny region sandwiched between the smallest interparticle spacings in each hot spot, while the intraparticle DYAB constituted the major product of the reaction. Despite their low abundance, the interparticle DYAB molecules might provide a significant contribution to the overall SERS signals because they were produced in the regions with the highest local-field enhancements. However, we were unable to further quantify

the exact fractions of the interparticle *vs.* intraparticle DYAB products because these two types of DYAB molecules were not readily distinguishable based on their SERS spectral features.

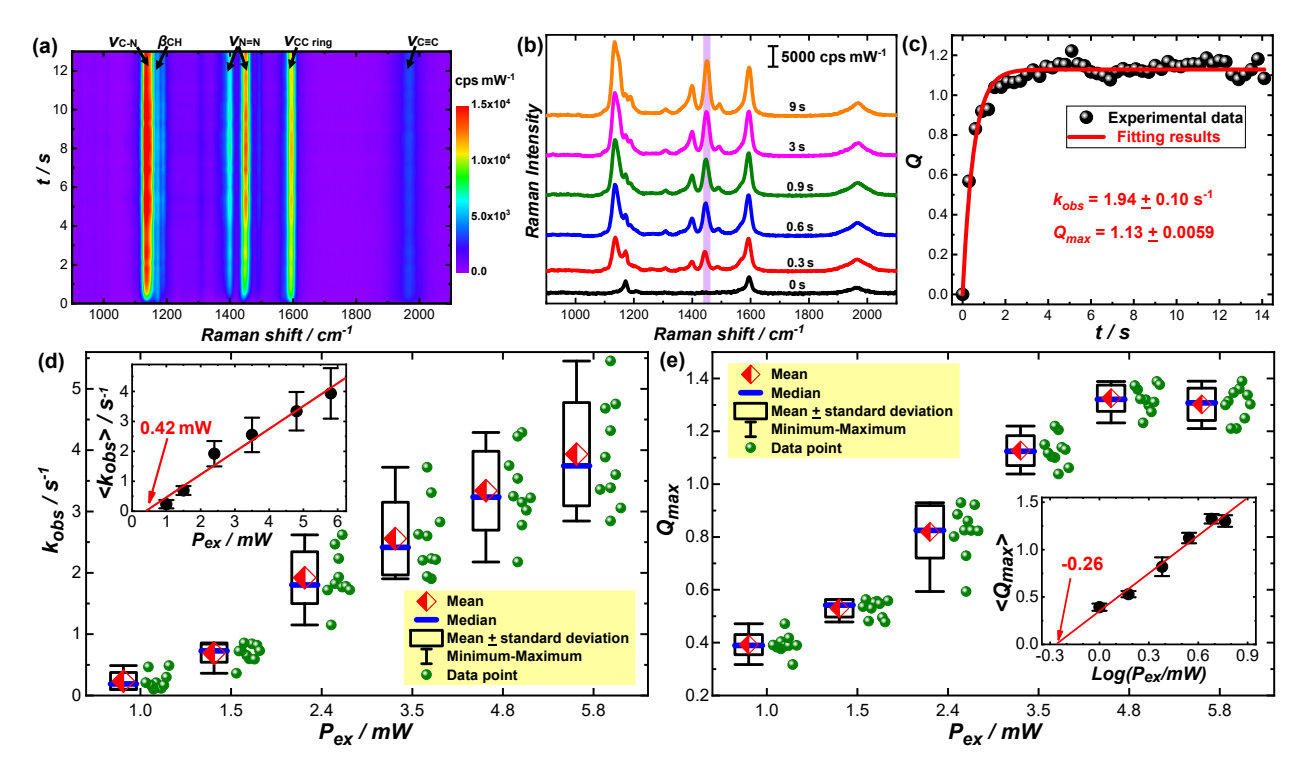


Figure 3. (a) Time-resolved SERS spectra during plasmon-driven oxidative coupling of pEA on an Ag NP substrate under 785 nm laser illumination in an aqueous solution at a pH of 13. The spectral acquisition time was 300 ms, and the laser power, P_{ex} , was 3.5 mW. (b) Snap-shot SERS spectra at reaction times of 0, 0.3, 0.6, 0.9, 3, and 9 s. The spectra are offset for clarity, and the Raman intensities are shown using the unit of counts per second per milliwatt (cps mW⁻¹). The SERS spectrum collected from a sample exposed to 100 mM ammonia borane was used to represent the spectrum at the reaction time of 0. (c) Temporal evolution of Q (the intensity ratio between the $v_{N=N}$ mode center at 1450 cm⁻¹ and the $v_{CC ring}$ mode centered at 1594 cm⁻¹) during plasmon-driven oxidative coupling of pEA on Ag at a P_{ex} of 3.5 mW. The kinetic results were fitted using Equation 2 and the fitting results are shown as a solid red curve. Box plots of (d) k_{obs} and (e) Q_{max} at various P_{ex} s. At each P_{ex} , the SERS-based kinetic measurements were repeated at 10 different spots on the Ag substrates. The insets show the P_{ex} -dependence of the ensemble-averaged k_{obs} , $< k_{obs}>$, and Q_{max} , $< Q_{max}>$. The results were fitted with linear functions and the x-intercepts were labeled in the inset panels.

We studied the reaction kinetics in detail by monitoring the temporal evolution of the reaction progress parameter, Q, which was defined as the intensity ratio between the strongest $v_{N=N}$ peak at 1450 cm⁻¹ and the $v_{CC ring}$ mode centered at 1594 cm⁻¹:

$$Q \equiv \frac{I(v_{N=N})}{I(v_{CC \, ring})}$$
 (Equation 1).

In our case, Q served as a descriptor of the apparent reaction progress, but not necessarily corresponded to the exact product fractions because the SERS intensities were related to not only the number of molecules but also the local-field enhancements in the hot spots. The field enhancements and the molecular packing densities on the Ag NP surfaces varied drastically from site to site, making it challenging to quantify the exact numbers of the reactant and product molecules residing in the hot spots. As shown in Figure 3c, the evolution of Q over the reaction time, t, could be well-described by a first-order rate law. The values of the apparent rate constant, k_{obs} , and maximal reaction yield achievable at an infinitely long reaction time, Q_{max} , were obtained by fitting the Q trajectory with the following rate equation:

$$Q(t) = Q_{max}(1 - e^{-k_{obs}t})$$
 (Equation 2).

We conducted the SERS-based kinetic measurements at various $P_{\rm ex}$ s, and at each $P_{\rm ex}$, the kinetic measurements were repeated at 10 different spots on the samples under identical reaction conditions. The Q trajectories collected form individual spots and the ensemble-averaged Q trajectories at various $P_{\rm ex}$ s are shown in Figures S6 and S7, respectively, in the Supplementary Information. In all cases, the temporal evolutions of Q followed the first-order kinetics, though the k_{obs} and Q_{max} values varied from site to site on each sample at each $P_{\rm ex}$. The site-to-site deviation in reaction kinetics stemmed from the heterogeneities of the local-field enhancements and the molecular distributions in the hot spots. The k_{obs} and Q_{max} values at individual spots on the samples at various $P_{\rm ex}$ s are shown as box plots in Figures 3d and 3e, respectively. In the $P_{\rm ex}$ range of 1-6 mW, both k_{obs} and Q_{max} values increased with $P_{\rm ex}$. At $P_{\rm ex}$ below 0.5 mW, the reactions became kinetically sluggish without any detectable production of DYAB after continuous laser illumination for several hours. As shown in the inset of Figure 3d, the ensemble-averaged k_{obs} ,

 $\langle k_{obs} \rangle$, increased linearly with P_{ex} , which was a typical kinetic feature of photocatalytic reactions driven by plasmonic hot carriers. 2,25,91 The linear relationship between $< k_{obs} >$ and P_{ex} also implied that photothermal heating had rather insignificant influence on the reaction rates.^{2,91} We chose thiophenol (TP) as a probe molecule with temperature-sensitive SERS features⁹²⁻⁹⁴ to measure the local surface temperatures in the hot spots during the plasmon-driven reactions. As shown in Figure S8a and S8b in Supplementary Information, the intensity ratios between the SERS peaks at 1000 and 1074 cm⁻¹, $I(1000 \text{ cm}^{-1})/I(1074 \text{ cm}^{-1})$, of TP chemisorbed to Ag NP surfaces exhibited a linear relationship to the temperature, which provided a working curve for Raman thermometry measurements. Because of the high thermal conductivity of H₂O (~0.6 W m⁻¹ K⁻¹), the heat generated through photothermal transduction was rapidly dissipated to the surroundings, resulting in limited local temperature elevation when the equilibrium between heat generation and dissipation was established. The steady-state local temperature in the hot spots only reached ~ 55 °C even when the P_{ex} was as high as 5.8 mW (Figure S8c and S8d in Supplementary Information). At a low $P_{\rm ex}$ of 0.30 mW, increasing the bulk reaction temperature to 55 °C did not lead to any significant kinetic enhancements (Figure S9 in Supplementary Information), further verifying that the kinetics of the pEA coupling reactions were primarily dictated by plasmonic photochemical effects rather than photothermal heating.

The power-dependence of $\langle k_{obs} \rangle$ shown in Figure 3d further implied that the surface-adsorbed pEA molecules could be activated for the coupling reactions only when the local field intensities exceeded a certain threshold value. When extrapolating the linear power dependence to k_{obs} of 0, we obtained a P_{ex} threshold value of 0.42 mW (corresponding to an excitation power density of 134 W mm⁻²) for this oxidative pEA coupling reactions. Increase in P_{ex} resulted in higher fractions of the molecules occupying the surface sites with local field intensities above the threshold value,

giving rise to increased Q_{max} values consequently. The ensemble-averaged Q_{max} , $< Q_{max}$, exhibited a linear relationship to the logarithm of $P_{\rm ex}$ (inset of Figure 3e), and extrapolation of the fitting result to Q_{max} of 0 yielded a threshold $log(P_{ex}/mW)$ value of -0.26, corresponding to a P_{ex} threshold of 0.55 mW, in agreement with the value extracted from the $P_{\rm ex}$ -dependence of $\langle k_{obs} \rangle$. These results indicated that the plasmon-driven pEA coupling on Ag NP surfaces required P_{ex} s above a threshold value of ~ 0.5 mW under our experimental conditions. Such excitation power thresholds have also been previously observed on other plasmon-driven molecule-transforming processes, such as the reductive coupling of pNTP⁹³ and decarboxylation of mercaptobenzobate⁹⁴ on Ag nanostructure surfaces. The threshold P_{ex} values may vary drastically from reaction to reaction, and are sensitively dependent upon the excitation wavelengths, local-field enhancements on the photocatalyst surfaces, and the local reaction environments. Takeyasu and coworkers⁵⁵ previously reported a threshold power density of 18.8 W mm⁻² for the pMA-to-DMAB conversion on aggregates Ag NPs at an excitation wavelength of 532 nm. Apparently, the plasmon-driven pEAcoupling under our reaction conditions required a P_{ex} threshold value remarkably higher than that for the pMA coupling under Takeyasu's reaction conditions.

Switching the molecular adsorbates from pEA to pMA gave rise to significantly higher reaction rates and more complicated kinetic profiles of the plasmon-driven oxidative coupling reactions. At a P_{ex} of 0.6 mW, pMA on Ag NP arrays underwent rapid coupling reactions to form DMAB (Figure 4a and 4b), whereas pEA on Ag NP arrays remained unreactive without forming DYAB at any detectable level. We identified two sub-populations of surface-adsorbed pMA featured by drastically different coupling kinetics. As shown in Figure 4c, the temporal evolution of Q (the intensity ratio between the $v_{N=N}$ mode center at 1436 cm⁻¹ and the $v_{CC ring}$ mode centered at 1578 cm⁻¹) was essentially the sum of two kinetic components as described by the following equation:

$$Q(t) = Q_{S,max}(1 - e^{-k_{S,obs}t}) + Q_{F,max}$$
 (Equation 3),

in which ks, obs was the apparent first-order rate constant of the slow-reacting subpopulation, and Qs_{max} and $Q_{F,max}$ represented the maximal yields achievable through the slow and fast coupling reactions, respectively. While the values of $ks_{,obs}$, $Qs_{,max}$, and $Q_{F,max}$ could all be obtained by fitting the Q trajectories using Equation 3, we were unable to further obtain the $k_{F,obs}$ values because the pMA-to-DMAB conversion for the fast kinetic component was fully accomplished within a time duration even shorter than the time resolution of our SERS measurements (200 ms). We systematically studied the kinetics of the pMA coupling reactions at various P_{ex} s in the range of 0.050-2.0 mW, and the two kinetic components were clearly distinguishable in all cases (Figures S10 and S11 in Supplementary Information). The values of ks_{obs} , Qs_{max} and $Q_{F,max}$ at various P_{exs} obtained through curve fitting of individual Q trajectories are shown as box plots with the ensemble-averaged values shown as inset panels in Figures 4d, 4e, and 4f, respectively. The $\langle ks,_{obs} \rangle$ increased linearly with P_{ex} until becoming saturated at P_{ex} above 1 mW (inset of Figure 4d). Extrapolation of the linear relationship to $\langle ks, obs \rangle$ of 0 yielded a $P_{\rm ex}$ threshold value of 7.3 \times 10^{-4} mW (corresponding to a power density of 232 mW mm⁻²) for the plasmon-driven pMA coupling reactions, about three orders of magnitude lower than that for the pEA coupling reactions. Although the $\langle Q_{max} \rangle$ values of pEA coupling reactions increased with P_{ex} (Figure 3e), both the $< Qs,_{max} >$ and $< Q_{F,max} >$ values for the pMA coupling reactions were observed to be independent of $P_{\rm ex}$ in the sub-mW $P_{\rm ex}$ regime. These results indicated that the threshold value of local-field intensities required for the activation of pMA was drastically lower than that for the pEA, and all the surface-adsorbed pMA molecules probed by SERS were successfully activated for the coupling reactions over the entire $P_{\rm ex}$ range explored in this work.

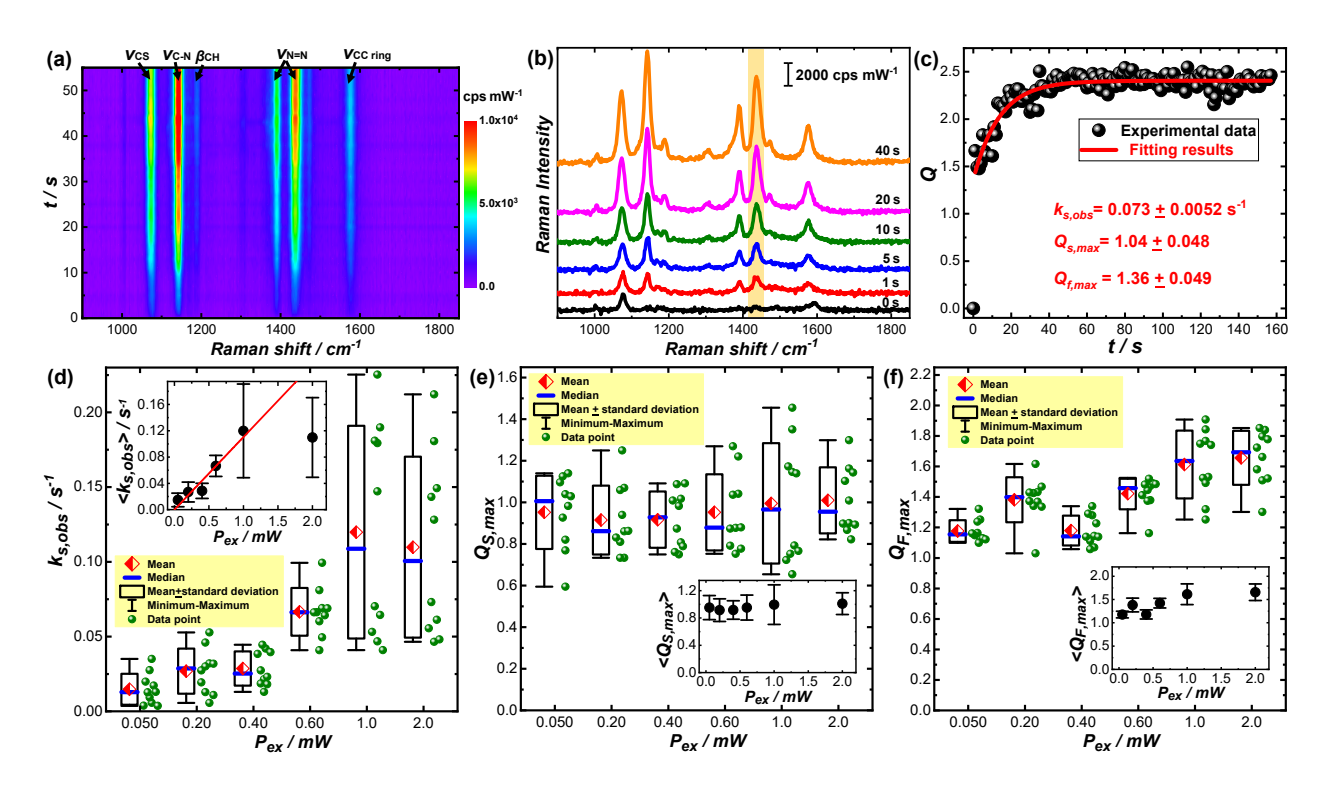


Figure 4. (a) Time-resolved SERS spectra during plasmon-driven oxidative coupling of pMA on an Ag NP substrate under 785 nm laser illumination in an aqueous solution at a pH of 13. The spectral acquisition time was 1 s, and the laser power, P_{ex} , was 0.6 mW. (b) Snap-shot SERS spectra at reaction times of 0, 1, 6, 10, 20, and 40 s. The SERS spectrum collected from a sample exposed to 100 mM ammonia borane was used to represent the spectrum at the reaction time of 0. (c) Temporal evolution of Q during plasmon-driven oxidative coupling of pMA on Ag at a P_{ex} of 0.6 mW. The kinetic results were fitted using Equation 3 and the fitting results are shown as a solid red curve. Box plots of (d) k_{obs} , (e) $Q_{S,max}$ and (e) $Q_{F,max}$ at various P_{ex} s. At each P_{ex} , the SERS-based kinetic measurements were repeated at 10 different spots on the Ag substrates. The insets show the P_{ex} -dependence of the ensemble-averaged k_{obs} , $Q_{S,max}$, and $Q_{F,max}$.

Our SERS results shown in Figures 3 and 4 clearly showed that the chemical nature of metal-adsorbate interactions was a key factor determining the kinetics of plasmon-driven oxidative coupling of aniline-derivatives. When altering the bonding nature of NP-adsorbate interactions, the Fermi level of the metal may be shifted with respect to the molecular orbitals of the adsorbates, thereby influencing the metal-to-adsorbate transfer of the plasmonic hot carriers. Under our reaction conditions, the plasmonic hot electrons were injected into the antibonding π^* orbital of

surface-adsorbed O₂ rather than the unoccupied orbitals of the aniline-derivative adsorbates. Therefore, the band alignment between the Fermi level and the molecular orbitals was unlikely to be the major reason causing the striking differences between pEA and pMA in terms of photochemical reactivities and coupling kinetics. The difference in coupling reaction kinetics could be most reasonably interpretated in the context of structural flexibility of the molecular adsorbates. The hybrid $\sigma\pi$ bonding nature of the Ag-ethynyl interactions restricted the motion of the surface-adsorbates, making pEA conformationally less flexible than its thiolated counterpart, pMA. Consequently, the pEA coupling reactions exhibited lower k_{obs} and Q_{max} and required a remarkably higher $P_{\rm ex}$ threshold than those of the pMA coupling reactions. The local surface curvature of the NPs was another key factor determining the structural flexibility of the molecular adsorbates. At the high-curvature surface sites, the molecular adsorbates were conformationally more flexible than those at the low-curvature surface sites, resulting in higher reactivity and faster reaction rates. Therefore, the fast and slow kinetic components resolved during plasmon-driven coupling of pMA reflected the transforming kinetics of pMA molecules residing at high-curvature and low-curvature sites, respectively, on the Ag NP surfaces. Our observations were well in line with the TERS results previously reported by Ren and coworkers, 61 who found that pMA on locally curved Ag NP surfaces underwent rapid coupling reactions to produce DMAB, whereas pMA on an atomically flat {111} Ag surface was completely unreactive. The plasmon-driven oxidative coupling of pEA only took place at the high-curvature sites when the $P_{\rm ex}$ exceeded the threshold value, whereas pEA molecules residing at the low-curvature sites remained unreactive because the conformational rigidity of the surface-adsorbed pEA inhibited the coupling between the amine groups. Therefore, only a single first-order kinetic component was observed during pEA coupling reactions.

The unreactive subpopulation of pEA at the low-curvature sites on Ag NP surfaces could be effectively activated when the conformationally more flexible pMA molecules were incorporated into the adsorbate monolayers. With a mixed pEA and pMA adsorbate layer on Ag NP surfaces, it became possible for a pEA molecule to couple with an adjacent pMA molecule, leading to the formation a heterodimer product, p,p'-mercaptoethynylazobenzene (MEAB) instead of the DYAB homodimers. We incubated the colloidal pEA-coated Ag NPs with various concentrations of pMA (C_{pMA}) for 2 h, after which the characteristic peaks of both the v_{CS} and $v_{C=C}$ modes became present in the SERS spectra (Figure 5a), verifying the co-adsorption of both pEA and pMA on the Ag NP surfaces. As C_{pMA} increased, the intensity ratios of the v_{CS} to the $v_{CC ring}$ modes, $I(v_{CS})/I(v_{CC ring})$, went up. We chose $I(v_{CS})/I(v_{CC ring})$ as an indicator for the apparent surface-coverage of pMA, $\theta_{pMA,app}$, based upon which an adsorption isotherm was obtained (Figure 5b). The adsorption behaviors of pMA onto the pEA-coated Ag NP surfaces could be well-described by a simple Langmuir binding isotherm:

$$\theta_{pMA,app} = \frac{I(v_{CS})}{I(v_{CC\,ring})} = \theta_{max} \frac{K_{pMA}C_{pMA}}{1 + K_{pMA}C_{pMA}} \quad \text{(Eqaution 4)},$$

in which K_{pMA} was the equalibrium constant for pMA binding, and θ_{max} was the maximal $\theta_{pMA,app}$ achievable at high pMA concentrations. $\theta_{pMA,app}$ increased with C_{pMA} until asymptotically approaching a θ_{max} value of ~ 0.28 (Figure 5b). With a saturated pMA monolayer coverage on Ag NP surfaces, the $I(v_{CS})/I(v_{CC \text{ ring}})$ value was measured to be 2.3 ± 0.2 based on the SERS results collected from pMA-coated Ag NP arrays (Figure 2c). Therefore, only a small fraction of pEA ($\sim 13\%$) could be displaced with pMA under our ligand exchange conditions. The peak intensity ratio between the $v_{C\equiv C}$ and $v_{CC \text{ ring}}$ modes, $I(v_{C\equiv C})/I(v_{CC \text{ ring}})$, gradually decreased as $\theta_{pMA,app}$ increased (Figure 5c). The $I(v_{C\equiv C})/I(v_{CC \text{ ring}})$ value decreased by $\sim 14\%$ after incubating the pEA-coated Ag NPs with 1 mM pEA for 2 h.

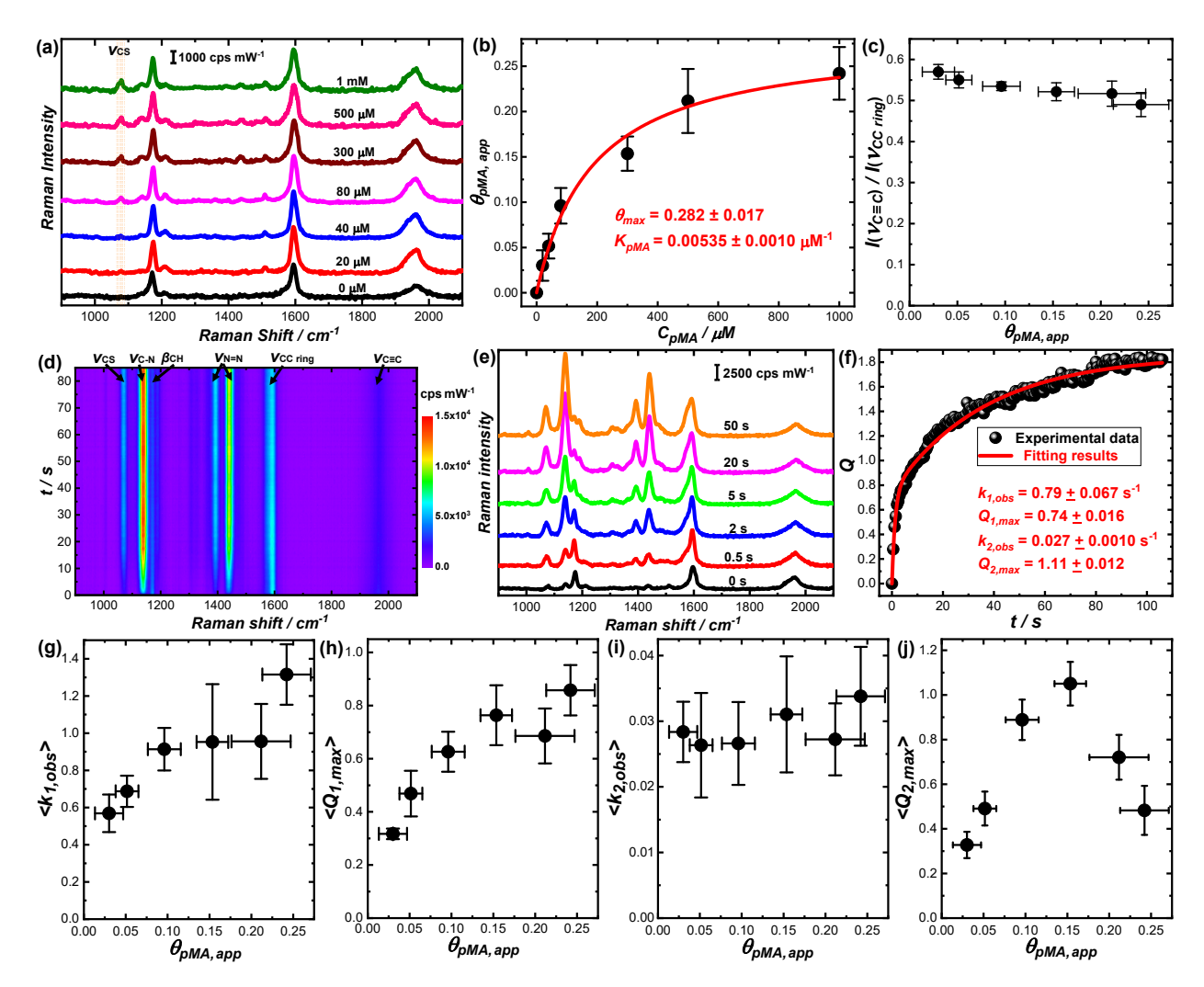


Figure 5. SERS spectra collected from pEA-coated Ag NP substrates after incubation with various concentrations of pMA for 2 h. When collecting the SERS data, the substrates were exposed to an aqueous solution of 100 mM ammonia borane to inhibit the plasmon-driven coupling reactions during the spectroscopic measurements. (b) Adsorption isotherm of pMA on pEA-coated Ag NP surfaces. The error bars represent the standard deviations of the results collected from 10 different spots on each sample. (c) Relationship between $I(v_{C=C})/I(v_{CC \text{ ring}})$ and $\theta_{pMA,app}$. (d) Time-resolved SERS spectra during plasmon-driven oxidative coupling of mixed pMA and pEA on an Ag NP substrate (pEA-coated Ag NPs were incubated with 300 μM of pMA for 2 h and then assembled into the close-packed array structures) in an aqueous solution at a pH of 13. The spectral acquisition time was 0.5 s, and the P_{ex} was 1.5 mW. (e) Snapshot SERS spectra at the reaction times of 0, 0.5, 2, 5, and 50 s. The SERS spectrum collected from a sample exposed to 100 mM ammonia borane was used to represent the spectrum at the reaction time of 0. (f) Temporal evolution of Q during plasmon-driven oxidative coupling of mixed pMA and pEA on Ag at a P_{ex} of 1.5 mW. The kinetic results were fitted using Equation 5 and the fitting results are shown as a solid red curve. Ensemble-averaged (g) $k_{l,obs}$, (h) $Q_{l,max}$, (i) $k_{2,obs}$, and (j) $Q_{2,max}$ of the plasmondriven oxidative coupling of mixed pEA and pMA on Ag NP substrates at different $\theta_{pMA,app}$. The SERS-based kinetic measurements were repeated at 10 different spots on each sample, and the error bars represent the standard deviations.

According to the results of DFT calculations, the three types of azo products, DMAB, MEAB, and DYAB all exhibited similar Raman spectral features in the wavenumber range of 1100-1700 cm⁻¹ except that the Raman peaks of the $v_{CC \text{ ring}}$ and $v_{N=N}$ modes slightly downshifted when switching from DYAB to MEAB and DMAB (Figure S12a in Supplementary Information). After continuous laser illumination of the mixed pMA and pEA adsorbates on the Ag NP substrates (pEA-coated Ag NPs incubated with 300 μ M pMA for 2 h) at a P_{ex} of 5.8 mW for 30 s, the reactive aniline-derivatives were fully converted into the azo compounds. Because only a small fraction of pEA was exchanged with pMA on the Ag NP surfaces (less than 7%), the probability of forming DMAB was expected to be rather limited. Therefore, the products of the coupling reactions were expected to be dominated by DYAB and MEAB. We observed that the SERS peaks of all the $v_{N=N}$ modes were downshifted with respect to those of DYAB produced through pEA coupling reactions, while the SERS peak of the $v_{CC ring}$ mode was asymmetrically broadened toward the lower wavenumber side (Figure S12b in Supplementary Information), indicating that both MEAB and DYAB were produced. When comparing the SERS spectra with the DFT results (Figure S13 in Supplementary Information), it became apparent that MEAB produced through the pEA-pMA coupling reactions were in the trans conformation rather than the cis conformation. Because of the limited spectral shifts and significant spectral overlap of the peaks, we were unable to further quantify the relative fractions of MEAB vs. DYAB based on the SERS results.

Time-resolved SERS measurements enabled us to obtain detailed kinetic and mechanistic information about the plasmon-driven oxidative coupling reactions occurring among intermixed pEA and pMA adsorbates on Ag NP surfaces. Figures 5d and 5e show the temporal evolution of the SERS spectra collected from intermixed pEA and pMA adsorbates on Ag NP surfaces (pEA-

coated Ag NPs were incubated with 300 μ M of pMA for 2 h and then assembled into the close-packed array structures) under continuous laser illumination at a P_{ex} of 1.5 mW. More detailed spectral features associated with the temporal evolution of the $v_{CC\ ring}$, $v_{C=C}$, and v_{CS} modes are highlighted in Figure S14 in Supporting Information. The SERS peaks of the $v_{CC\ ring}$ modes of the DYAB and MEAB were centered at 1594 cm⁻¹ and ~1580 cm⁻¹, respectively. As the coupling reactions proceeded, the $v_{CC\ ring}$ peak, originally centered at 1594 cm⁻¹, became asymmetrically broadened as a shoulder at ~1580 cm⁻¹ was progressively developed, indicating that both DYAB and MEAB were produced during the coupling reactions. Both the peak positions and lineshapes of the $v_{C=C}$ mode remained essentially unchanged, suggesting minimal orientation changes of the C=C triple bond in the ethynyl group during the coupling reactions. Although no spectral shift of the v_{CS} mode was observed, the intensity of the v_{CS} peak progressively went up during the reactions because MEAB had larger Raman cross-sections than those of pMA. As shown in Figure 5c, the temporal evolutionary profile of Q could be fully described as the sum of two kinetic components, each of which obeyed a first-order rate law:

$$Q(t) = Q_{1,max}(1 - e^{-k_{1,obs}t}) + Q_{2,max}(1 - e^{-k_{2,obs}t})$$
 (Equation 5),

where $k_{I,obs}$ and $Q_{I,max}$ were the apparent rate constant and maximal reaction yield for the fast coupling reactions at the high-curvature surface sites, while $k_{2,obs}$ and $Q_{2,max}$ were the apparent rate constant and maximal reaction yield for the slow coupling reactions at the low-curvature surface sites. While both MEAB and DYAB could be produced at the high-curvature sites, the products at the low-curvature sites were dominated by MEAB only because of limited conformational flexibility and reactivity of surface-adsorbed pEA. At the same $P_{ex}s$, the pEA-pMA coupling reactions at the low-curvature sites were found to be significantly slower than the pMA-pMA coupling reactions. At a fixed P_{ex} of 1.5 mW, we systematically studied the kinetics of the coupling

reactions among intermixed pEA and pMA adsorbates as a function of pMA surface coverage, and at each $\theta_{pMA,app}$, the time-resolved SERS measurements were repeated at 10 different spots on each sample (Figures S15 and S16 in Supplementary Information). The $k_{1,obs}$, $Q_{1,max}$, $k_{2,obs}$, and $Q_{2,max}$ values extracted from the curve-fitting results are shown as box plots in Figure S17 in Supplementary Information. The ensemble-averaged $k_{1,obs}$ and $Q_{1,max}$ values both increased with the $\theta_{pMA,app}$ (Figure 5g and 5h), indicating that the incorporation of pMA onto the Ag NP surfaces further promoted the oxidative coupling reactions at the high-curvature surface sites. In contrast, the ensemble-averaged $k_{2,obs}$ values appeared almost independent of $\theta_{pMA,app}$ (Figure 5i), suggesting that the orientational change of pMA served as the rate-limiting step during the pEA-pMA coupling reactions at the low-curvature surfaces sites. Interestingly, the ensemble-averaged $Q_{2,max}$ exhibited a volcano-type relationship to $\theta_{pMA,app}$, and the highest $\langle Q_{2,max} \rangle$ values were achieved at $\theta_{pMA,app}$ around 0.15 (Figure 5j). We hypothesized that as $\theta_{pMA,app}$ exceeded a certain level, pMA molecules might start to accumulate locally and form structurally ordered and rigid domains on the Ag NP surfaces, which caused the decrease of $Q_{2,max}$. We also attempted to create intermixed pEA and pMA adsorbates on Ag NP surfaces by incubating pMA-coated Ag NPs with pEA solutions (Figure S18 in Supplementary Information). In this case, only a very limited fraction of surface-bound pMA was displaced by pEA even at pEA concentrations as high as 1 mM (the $v_{C=C}$ mode was almost undetectable in the SERS spectrum after ligand exchange). The incorporation of trace amount of pEA into the pMA adsorbate layer did not cause any significant changes to the kinetics of the fast reactions at the high-curvature sites. However, the slow coupling reactions occurring at the low-curvature sites became even slower because the activation energy barrier for the MEAB formation was higher than that for the DMAB formation.

CONCLUSION

This work focused on systematic comparison of the plasmon-driven transforming behaviors of an alkynylated aniline-derivative, pEA, and a thiolated aniline-derivative, pMA, chemisorbed to Ag NP surfaces, which allowed us to correlate the conformations and conformational flexibility of the adsorbates to the photochemical reactivity and molecule-transforming kinetics during plasmon-driven oxidative coupling reactions. Time-resolved SERS was used as an in situ spectroscopic tool to fine-resolve the detailed structural evolution of the aniline-derivative adsorbates during the plasmon-driven coupling reactions, and the experimental results were further corroborated by DFT calculations. While the σ-bonding nature of Ag-thiol interactions created certain level of conformational flexibility of surface-adsorbed pMA, an ethynyl group interacted with Ag through a hybrid $\sigma\pi$ -bonding mode, forcing the C \equiv C bond in pEA to lean toward the Ag surfaces with restricted freedom of conformational changes. Therefore, pEA exhibited decreased photochemical reactivities and slower coupling rates in comparison to pMA under identical photocatalytic reaction conditions. The structural flexibility of the adsorbates was also dependent upon the local surface curvature of the NPs. While the pMA molecules underwent rapid coupling reactions at the high-curvature surface sites, the reactions became significantly slower at the lowcurvature sites as the adsorbate molecules became more densely packed and thus structurally less flexible. In contrast, the plasmon-driven pEA coupling reaction occurred only at the high-curvature sites, whereas the pEA molecules residing at the low-curvature sites remained essentially unreactive due to limited conformational flexibility. When certain fractions of surface-adsorbed pEA were exchanged with pMA, the originally unreactive pEA at the low-curvature sites became reactivate, forming a heterodimer product, MEAB, through pEA-pMA coupling reactions. The results reported in this work shed light on the crucial roles of the metal-adsorbate interactions in

kinetic modulation of plasmon-driven photocatalytic reactions, implying that in addition to the plasmonic characteristics of the photocatalysts, the structures of the molecular adsorbates should also be deliberately tailored when optimizing plasmon-mediated molecule-transforming processes.

METHODS

Chemicals and Materials. Silver nitrate (AgNO₃, \geq 99.0%), pEA (C₈H₇N, 97%), pMA (C₆H₇NS, 97%), sodium borohydride (NaBH₄, 99.99% trace metals basis), ascorbic acid (C₆H₈O₆, AA, \geq 95%), and ITO-coated glass substrates were purchased from Sigma Aldrich. Thiophenol (C₆H₆S, TP, 99+%) and cetyltrimethylammonium chloride (C₁₉H₄₂NCl, CTAC, 96%) were purchased from Alfa Aesar. All reagents were used as received without further purification. Ultrapure water (18.2 M Ω resistivity, Barnstead) was used for all the experiments associated with nanostructure synthesis and sample preparation.

Synthesis of Ag NPs. Colloidal Ag NPs with an average diameter of 45 nm were synthesized following a previously reported protocol. Solloidal Ag seeds were first synthesized by adding 25 μL of 100 mM AgNO₃ and 450 μL of 20 mM NaBH₄ into 10 mL of 0.5 mM CTAC in an aqueous solution under magnetic stir. The reactant mixtures were kept at 30 °C for 40 min. Then 100 μL of the as-prepared seeds and 100 μL of 100 mM AgNO₃ was added to 88 mL of an aqueous solution containing 20 mM CTAC. After keeping the reactant mixture at 60 °C for 20 min, 1 mL of 100 mM AA was added, and the mixture was kept at 60 °C for another 3 h. Finally, 100 μL of 10 mM Cu(NO₃)₂ was introduced into the reactant mixture to etch the sharp vertices and edges of the Ag NPs. After further reaction for 1 h, colloidal Ag NPs with a uniform quasi-spherical particle morphology and a narrow size distribution were synthesized. The Ag NPs were centrifuged, washed with water three times, and finally redispersed in water for future use.

Time-Resolved SERS Measurements. The SERS spectra were collected from molecular adsorbates on close-packed Ag NPs arrays supported by ITO-coated glass substrates. The assynthesized Ag NPs were incubated with 1.0 mM of pATP or pEA at room temperature for 2 h to ensure the complete displacement of CTAC with the target aniline-derivative adsorbates. For the ligand exchange between pEA and pMA, the pEA-coated colloidal Ag NPs were incubated with various concentrations of pMA for 2 h at room temperature. After the ligand exchange processes, the colloidal Ag NPs were centrifuged and redispersed in water. The Ag NPs coated with various molecular adsorbates were assembled into close-packed arrays through slow solvent evaporation of aqueous colloidal inks on ITO-coated glass substrates at room temperature.

Time-resolved SERS spectra were collected using a BaySpec NomadicTM confocal Raman microscope built on an Olympus BX51 reflected optical system under 785 nm laser excitation in the confocal mode (focal spot size: 2 μm in diameter). A 50× dark field objective (NA = 0.5, WD = 10.6 mm, Olympus LMPLFLN-BD) was used for both Raman signal collection and dark-field imaging. The Raman signals were collected in a back scattering configuration. The laser power was controlled between 0.03 - 6 mW by using neutral density filters, and the integration time for most conditions varied in the range of 0.3-1 s. A homebuilt reaction chamber⁸⁹ was assembled on top of the ITO-supported Ag NP arrays, and an aqueous medium containing 100 mM KOH (pH = 13) was continuous flowed into the reaction chamber at a constant flow rate of 1 μL min⁻¹.

DFT Calculations. DFT calculations were performed using QChem 5.4 software package, with the functional of B3LYP applied in all calculations. The 6-31+G** basis set was used for non-metal atoms, while the def2-ecp basis set was used for the Ag atoms and their effective core potential. The polarizable continuum model (PCM) was used as the solvation model. The medium surrounding the molecules was water, whose dielectric constant was set to be 78.39. The Raman

activities obtained from the output files were converted to relative Raman intensities according to the equation below:⁹⁶

$$I_{i} = \frac{f (v_{0} - v_{i})^{4} S_{i}}{v_{i} \left[1 - exp\left(-\frac{hcv_{i}}{k_{b}T}\right)\right]}$$
(Equation 6),

where v_0 was the frequency of the excitation laser, v_i was the vibrational frequency of the i^{th} normal mode, h was the Planck constant, c was the speed of light in a vacuum, k_0 was the Boltzmann constant, and S_i was the Raman activity of the i^{th} normal mode. f was an appropriately chosen common scaling factor for all peak intensities. In our calculations, the excitation frequency was set at 12738.85 cm⁻¹, which corresponded to an excitation wavelength of 785 nm. A scaling factor of 1 was used for all the peak intensities, and the temperature was set at 298.15 K. The Raman intensity were expanded with Lorentzian line shape. A full width at half-maximum (fwhm) of 7 cm⁻¹ was used for all the Raman peaks.

Structural Characterizations. TEM images were obtained using a Hitachi HT-7800 transmission electron microscope operated at an accelerating voltage of 120 kV. SEM images were taken using a Zeiss Gemini500 field emission scanning electron microscope. The optical extinction spectra were collected from colloidal NP suspensions or Ag NP arrays on ITO-coated glass substrates using a Beckman Coulter Du 640 spectrophotometer. Optical dark-field microscopy images of the SERS substrates were taken using an Olympus BX51 optical microscope, which was integrated with the confocal Raman microscope.

ASSOCIATED CONTENT

Supplementary Information. Additional figures as noted in the maintext, including SERS spectra, detailed kinetic results, and Raman thermometry results.

ACKNOWLEDGMENT

This material is based upon work supported primarily by the National Science Foundation under Grants CHE-2202928 (chemistry and photochemistry on metallic nanoparticle surfaces) and OIA-1655740 (hierarchical assembly of nanoparticles) and in part by the University of South Carolina (UofSC) Office of Vice President for Research through an ASPIRE-I Track-IV award. K.C. was partially supported by a UofSC SPARC Award. The Zeiss Gemini500 thermal field emission scanning electron microscope used in this work was purchased using the South Carolina STEM Equipment Funds.

AUTHOR DECLARATIONS

Conflict of Interest

The authors have no conflicts to disclose.

Author Contributions

K.C. collected the experimental data and did the DFT calculations. K.C and H.W. analyzed the data. H.W. designed the project, supervised the research, acquired funding support, and wrote the paper. Both authors have given approval to the final version of the manuscript.

DATA AVAILABILITY

The data that support the findings of this study are available within the article and its supplementary material.

REFERENCES

- ¹ M. L. Brongersma, N. J. Halas, and P. Nordlander, Nat. Nanotech. 10 (1), 25 (2015).
- ² M. J. Kale, T. Avanesian, and P. Christopher, ACS Catal. 4 (1), 116 (2014).
- ³ S. Linic, U. Aslam, C. Boerigter, and M. Morabito, Nat. Mater. **14** (6), 567 (2015).
- ⁴ A. O. Govorov, H. Zhang, H. V. Demir, and Y. K. Gun'ko, Nano Today **9** (1), 85 (2014).
- ⁵ P. Christopher and M. Moskovits, Annu. Rev. Phys. Chem. **68**, 379 (2017).
- ⁶ J. Gargiulo, R. Berte, Y. Li, S. A. Maier, and E. Cortes, Acc. Chem. Res. **52** (9), 2525 (2019).
- ⁷ E. Kazuma and Y. Kim, Angew. Chem. Inter. Ed. **58** (15), 4800 (2019).
- ⁸ Z. L. Zhang, C. Y. Zhang, H. R. Zheng, and H. X. Xu, Acc. Chem. Res. **52** (9), 2506 (2019).
- ⁹ I. Kherbouche, Y. Luo, N. Felidj, and C. Mangeney, Chem. Mater. **32** (13), 5442 (2020).
- ¹⁰ C. Zhan, M. Moskovits, and Z. Q. Tian, Matter **3** (1), 42 (2020).
- A. Gelle, T. Jin, L. de la Garza, G. D. Price, L. V. Besteiro, and A. Moores, Chem. Rev. 120 (2), 986 (2020).
- Y. C. Zhang, S. He, W. X. Guo, Y. Hu, J. W. Huang, J. R. Mulcahy, and W. D. Wei, Chem. Rev. 118 (6), 2927 (2018).
- ¹³ E. Kazuma, J. Jung, H. Ueba, M. Trenary, and Y. Kim, Science **360** (6388), 521 (2018).
- ¹⁴ E. Miliutina, O. Guselnikova, N. S. Soldatova, P. Bainova, R. Elashnikov, P. Fitl, T. Kurten, M. S. Yusubov, V. Svorcik, R. R. Valiev, M. M. Chehimi, O. Lyutakov, and P. S. Postnikov, J. Phys. Chem. Lett. 11 (14), 5770 (2020).
- ¹⁵ R. Schurmann and I. Bald, Nanoscale **9** (5), 1951 (2017).
- ¹⁶ T. E. Tesema, B. Kafle, M. G. Tadesse, and T. G. Habteyes, J. Phys. Chem. C **121** (13), 7421 (2017).
- ¹⁷ C. Boerigter, R. Campana, M. Morabito, and S. Linic, Nat. Commun. 7, 10545 (2016).

- ¹⁸ H. K. Choi, K. S. Lee, H. H. Shin, and Z. H. Kim, J. Phys. Chem. Lett. **7** (20), 4099 (2016).
- ¹⁹ P. Christopher, H. L. Xin, and S. Linic, Nat. Chem. **3** (6), 467 (2011).
- ²⁰ S. Mukherjee, F. Libisch, N. Large, O. Neumann, L. V. Brown, J. Cheng, J. B. Lassiter, E. A. Carter, P. Nordlander, and N. J. Halas, Nano Lett. **13** (1), 240 (2013).
- ²¹ W. Xie and S. Schlucker, Nat. Commun. **6**, 7570 (2015).
- ²² Y. Dubi, I. W. Un, and Y. Sivan, Chem. Sci. **11** (19), 5017 (2020).
- ²³ A. A. Golubev, B. N. Khlebtsov, R. D. Rodriguez, Y. Chen, and D. R. T. Zahn, J. Phys. Chem. C 122 (10), 5657 (2018).
- ²⁴ F. Wang, C. H. Li, H. J. Chen, R. B. Jiang, L. D. Sun, Q. Li, J. F. Wang, J. C. Yu, and C. H. Yan, J. Am. Chem. Soc. 135 (15), 5588 (2013).
- ²⁵ K. X. Chen and H. Wang, Mole. Syst. Des. Eng. **6** (4), 250 (2021).
- ²⁶ E. Cortes, L. V. Besteiro, A. Alabastri, A. Baldi, G. Tagliabue, A. Demetriadou, and P. Narang, ACS Nano **14** (12), 16202 (2020).
- ²⁷ X. Q. Li, H. O. Everitt, and J. Liu, Nano Res. **13** (5), 1268 (2020).
- ²⁸ Y. Sivan, J. Baraban, I. W. Un, and Y. Dubi, Science **364** (6439), eaaw9367 (2019).
- ²⁹ T. E. Tesema, B. Kafle, and T. G. Habteves, J. Phys. Chem. C **123** (14), 8469 (2019).
- 30 X. Zhang, X. Q. Li, M. E. Reish, D. Zhang, N. Q. Su, Y. Gutierrez, F. Moreno, W. T. Yang, H.
 O. Everitt, and J. Liu, Nano Lett. 18 (3), 1714 (2018).
- ³¹ L. A. Zhou, D. F. Swearer, C. Zhang, H. Robatjazi, H. Q. Zhao, L. Henderson, L. L. Dong, P. Christopher, E. A. Carter, P. Nordlander, and N. J. Halas, Science 362 (6410), 69 (2018).
- ³² K. Kneipp, H. Kneipp, I. Itzkan, R. R. Dasari, and M. S. Feld, Chem. Rev. **99** (10), 2957 (1999).
- J. Langer, D. J. de Aberasturi, J. Aizpurua, R. A. Alvarez-Puebla, B. Auguie, J. J. Baumberg, G.
 C. Bazan, S. E. J. Bell, A. Boisen, A. G. Brolo, J. Choo, D. Cialla-May, V. Deckert, L. Fabris,

- K. Faulds, F. J. G. de Abajo, R. Goodacre, D. Graham, A. J. Haes, C. L. Haynes, C. Huck, T. Itoh, M. Ka, J. Kneipp, N. A. Kotov, H. Kuang, E. C. Le Ru, H. K. Lee, J. F. Li, X. Y. Ling, S. A. Maier, T. Mayerhofer, M. Moskovits, K. Murakoshi, J. M. Nam, S. Nie, Y. Ozaki, I. Pastoriza-Santos, J. Perez-Juste, J. Popp, A. Pucci, S. Reich, B. Ren, G. C. Schatz, T. Shegai, S. Schlucker, L. L. Tay, K. G. Thomas, Z. Q. Tian, R. P. Van Duyne, T. Vo-Dinh, Y. Wang, K. A. Willets, C. Xu, H. Xu, Y. Xu, Y. S. Yamamoto, B. Zhao, and L. M. Liz-Marzan, ACS Nano 14 (1), 28 (2020).
- ³⁴ B. Sharma, R. R. Frontiera, A. I. Henry, E. Ringe, and R. P. Van Duyne, Mater. Today **15** (1-2), 16 (2012).
- ³⁵ S. Y. Ding, J. Yi, J. F. Li, B. Ren, D. Y. Wu, R. Panneerselvam, and Z. Q. Tian, Nat. Rev. Mater. 1 (6) (2016).
- ³⁶ R. M. Stockle, Y. D. Suh, V. Deckert, and R. Zenobi, Chem. Phys. Lett. **318** (1-3), 131 (2000).
- ³⁷ R. Zhang, Y. Zhang, Z. C. Dong, S. Jiang, C. Zhang, L. G. Chen, L. Zhang, Y. Liao, J. Aizpurua, Y. Luo, J. L. Yang, and J. G. Hou, Nature 498 (7452), 82 (2013).
- ³⁸ A. B. Zrimsek, N. H. Chiang, M. Mattei, S. Zaleski, M. O. McAnally, C. T. Chapman, A. I. Henry, G. C. Schatz, and R. P. Van Duyne, Chem. Rev. **117** (11), 7583 (2017).
- ³⁹ C. Zhan, X. J. Chen, Y. F. Huang, D. Y. Wu, and Z. Q. Tian, Acc. Chem. Res. **52** (10), 2784 (2019).
- ⁴⁰ S. Schlucker, Angew. Chem. Inter. Ed. **53** (19), 4756 (2014).
- ⁴¹ E. M. van Schrojenstein Lantman, T. Deckert-Gaudig, A. J. G. Mank, V. Deckert, and B. M. Weckhuysen, Nat. Nanotech. **7** (9), 583 (2012).
- ⁴² X. J. Chen, G. Cabello, D. Y. Wu, and Z. Q. Tian, J. Photochem. Photobiol. C 21, 54 (2014).

- ⁴³ H. K. Choi, W. H. Park, C. G. Park, H. H. Shin, K. S. Lee, and Z. H. Kim, J. Am. Chem. Soc. **138** (13), 4673 (2016).
- ⁴⁴ M. Osawa, N. Matsuda, K. Yoshii, and I. Uchida, J. Phys. Chem. **98** (48), 12702 (1994).
- ⁴⁵ X. M. Yang, D. A. Tryk, K. Ajito, K. Hashimoto, and A. Fujishima, Langmuir **12** (23), 5525 (1996).
- ⁴⁶ X. M. Yang, D. A. Tryk, K. Hashimoto, and A. Fujishima, J. Raman Spectroscopy **29** (8), 725 (1998).
- ⁴⁷ Y. Z. Huang, Y. R. Fang, Z. L. Yang, and M. T. Sun, J. Phys. Chem. C **114** (42), 18263 (2010).
- ⁴⁸ H. K. Choi, H. K. Shon, H. Yu, T. G. Lee, and Z. H. Kim, J. Phys. Chem. Lett. **4** (7), 1079 (2013).
- ⁴⁹ Y. R. Fang, Y. Z. Li, H. X. Xu, and M. T. Sun, Langmuir **26** (11), 7737 (2010).
- ⁵⁰ K. Kim, K. L. Kim, D. Shin, J. Y. Choi, and K. S. Shin, J. Phys. Chem. C **116** (7), 4774 (2012).
- ⁵¹ D. Y. Wu, X. M. Liu, Y. F. Huang, B. Ren, X. Xu, and Z. Q. Tian, J. Phys. Chem. C 113 (42), 18212 (2009).
- ⁵² Y. F. Huang, H. P. Zhu, G. K. Liu, D. Y. Wu, B. Ren, and Z. Q. Tian, J. Am. Chem. Soc. **132** (27), 9244 (2010).
- ⁵³ P. Xu, L. L. Kang, N. H. Mack, K. S. Schanze, X. J. Han, and H. L. Wang, Sci. Rep. 3, 2997 (2013).
- ⁵⁴ M. T. Sun, Y. Z. Huang, L. X. Xia, X. W. Chen, and H. X. Xu, J. Phys. Chem. C 115 (19), 9629 (2011).
- ⁵⁵ N. Takeyasu, R. Kagawa, K. Sakata, and T. Kaneta, J. Phys. Chem. C **120** (22), 12163 (2016).
- ⁵⁶ Y. F. Huang, M. Zhang, L. B. Zhao, J. M. Feng, D. Y. Wu, B. Ren, and Z. Q. Tian, Angew. Chem. Inter. Ed. **53** (9), 2353 (2014).

- ⁵⁷ J. Y. Chu, P. Miao, X. J. Han, Y. C. Du, X. J. Wang, B. Song, and P. Xu, ChemCatChem 8 (10), 1819 (2016).
- ⁵⁸ C. Zhan, Z. Y. Wang, X. G. Zhang, X. J. Chen, Y. F. Huang, S. Hu, J. F. Li, D. Y. Wu, M. Moskovits, and Z. Q. Tian, J. Am. Chem. Soc. **141** (20), 8053 (2019).
- ⁵⁹ L. B. Zhao, M. Zhang, Y. F. Huang, C. T. Williams, D. Y. Wu, B. Ren, and Z. Q. Tian, J. Phys. Chem. Lett. 5 (7), 1259 (2014).
- ⁶⁰ Q. Zhang and H. Wang, J. Phys. Chem. C **122** (10), 5686 (2018).
- ⁶¹ J. J. Sun, H. S. Su, H. L. Yue, S. C. Huang, T. X. Huang, S. Hu, M. M. Sartin, J. Cheng, and B. Ren, J. Phys. Chem. Lett. **10** (10), 2306 (2019).
- W. Koopman, E. Titov, R. M. Sarhan, T. Gaebel, R. Schurmann, A. Mostafa, S. Kogikoski, F. Stete, F. Liebig, C. N. Z. Schmitt, J. Koetz, I. Bald, P. Saalfrank, M. Bargheer, and A. R. Milosavjevio, Adv. Mater. Interfaces 8 (22) (2021).
- ⁶³ Z. F. Cai, J. P. Merino, W. Fang, N. Kumar, J. O. Richardson, S. De Feyter, and R. Zenobi, J. Am. Chem. Soc. **144** (1), 538 (2022).
- ⁶⁴ J. Pinson and F. Podvorica, Chem. Soc. Rev. **34** (5), 429 (2005).
- 65 C. Cao, Y. Zhang, C. Jiang, M. Qi, and G. Z. Liu, ACS Appl. Mater. Interfaces 9 (6), 5031 (2017).
- ⁶⁶ J. K. Kariuki and M. T. McDermott, Langmuir **17** (19), 5947 (2001).
- ⁶⁷ L. Laurentius, S. R. Stoyanov, S. Gusarov, A. Kovalenko, R. B. Du, G. P. Lopinski, and M. T. McDermott, ACS Nano 5 (5), 4219 (2011).
- ⁶⁸ A. A. Mohamed, Z. Salmi, S. A. Dahoumane, A. Mekki, B. Carbonnier, and M. M. Chehimi, Adv. Coll. Interface Sci. **225**, 16 (2015).
- ⁶⁹ A. Mesnage, X. Lefevre, P. Jegou, G. Deniau, and S. Palacin, Langmuir **28** (32), 11776 (2012).

- ⁷⁰ R. Ahmad, L. Boubekeur-Lecaque, M. Nguyen, S. Lau-Truong, A. Lamouri, P. Decorse, A. Galtayries, J. Pinson, N. Felidj, and C. Mangeney, J. Phys. Chem. C **118** (33), 19098 (2014).
- ⁷¹ X. M. Han, H. K. Lee, Y. H. Lee, W. Hao, Y. J. Liu, I. Y. Phang, S. Z. Li, and X. Y. Ling, J. Phys. Chem. Lett. **7** (8), 1501 (2016).
- ⁷² S. A. Swanson, R. McClain, K. S. Lovejoy, N. B. Alamdari, J. S. Hamilton, and J. C. Scott, Langmuir **21** (11), 5034 (2005).
- J. J. Stapleton, T. A. Daniel, S. Uppili, O. M. Cabarcos, J. Naciri, R. Shashidhar, and D. L. Allara, Langmuir 21 (24), 11061 (2005).
- ⁷⁴ S. W. Joo, W. J. Kim, W. S. Yoon, and I. S. Choi, J. Raman Spectroscopy **34** (4), 271 (2003).
- J. I. Henderson, S. Feng, G. M. Ferrence, T. Bein, and C. P. Kubiak, Inorg. Chim. Acta 242 (1-2), 115 (1996).
- ⁷⁶ S. Shi, Y. D. Zhang, J. Ahn, and D. Qin, Chem. Sci. **11** (41), 11214 (2020).
- ⁷⁷ J. Ahn, S. Shi, B. Vannatter, and D. Oin, J. Phys. Chem. C **123** (35), 21571 (2019).
- ⁷⁸ C. M. Crudden, J. H. Horton, I. I. Ebralidze, O. V. Zenkina, A. B. McLean, B. Drevniok, Z. She, H.-B. Kraatz, N. J. Mosey, T. Seki, E. C. Keske, J. D. Leake, A. Rousina-Webb, and G. Wu, Nat. Chem. 6 (5), 409 (2014).
- ⁷⁹ M. N. Hopkinson, C. Richter, M. Schedler, and F. Glorius, Nature **510** (7506), 485 (2014).
- ⁸⁰ C. M. Crudden, J. H. Horton, M. R. Narouz, Z. Li, C. A. Smith, K. Munro, C. J. Baddeley, C. R. Larrea, B. Drevniok, B. Thanabalasingam, A. B. McLean, O. V. Zenkina, I. I. Ebralidze, Z. She, H.-B. Kraatz, N. J. Mosey, L. N. Saunders, and A. Yagi, Nature Commun. 7, 12654 (2016).
- 81 A. V. Zhukhovitskiy, M. G. Mavros, T. Van Voorhis, and J. A. Johnson, J. Am. Chem. Soc. 135 (20), 7418 (2013).

- ⁸² J. F. DeJesus, M. J. Trujillo, J. P. Camden, and D. M. Jenkins, J. Am. Chem. Soc. **140** (4), 1247 (2018).
- ⁸³ M. J. Trujillo, S. L. Strausser, J. C. Becca, J. F. DeJesus, L. Jensen, D. M. Jenkins, and J. P. Camden, J. Phys. Chem. Lett. **9** (23), 6779 (2018).
- 84 D. Fracasso, S. Kumar, P. Rudolf, and R. C. Chiechi, RSC Adv. 4 (99), 56026 (2014).
- 85 Y. H. Feng, S. X. Xing, J. Xu, H. Wang, J. W. Lim, and H. Y. Chen, Dalton Trans. 39 (2), 349 (2010).
- ⁸⁶ H. Feilchenfeld and M. J. Weaver, J. Phys. Chem. **93** (10), 4276 (1989).
- ⁸⁷ P. Maity, S. Takano, S. Yamazoe, T. Wakabayashi, and T. Tsukuda, J. Am. Chem. Soc. **135** (25), 9450 (2013).
- ⁸⁸ Y. Liu, C. Q. Ma, Y. Q. Yang, Y. C. Zhao, S. W. Wu, J. Wang, P. Song, and L. X. Xia, RSC Adv. 8 (37), 20499 (2018).
- ⁸⁹ H. Wang, K. Musier-Forsyth, C. Falk, and P. F. Barbara, J. Phys. Chem. B **117** (16), 4183 (2013).
- ⁹⁰ Y. F. Huang, D. Y. Wu, H. P. Zhu, L. B. Zhao, G. K. Liu, B. Ren, and Z. Q. Tian, Phys. Chem. Phys. **14** (24), 8485 (2012).
- ⁹¹ Y. Sivan, J. H. Baraban, and Y. Dubi, OSA Continuum **3** (3), 483 (2020).
- 92 R. L. Aggarwal, L. W. Farrar, and S. K. Saikin, J. Phys. Chem. C **116** (31), 16656 (2012).
- ⁹³ Q. F. Zhang, Y. D. Zhou, X. Q. Fu, E. Villarreal, L. C. Sun, S. L. Zou, and H. Wang, J. Phys. Chem. C 123 (43), 26695 (2019).
- ⁹⁴ Q. F. Zhang, K. X. Chen, and H. Wang, J. Phys. Chem. C **125** (38), 20958 (2021).
- ⁹⁵ X. Lin, S. Lin, Y. L. Liu, M. M. Gao, H. Y. Zhao, B. K. Liu, W. Hasi, and L. Wang, Langmuir 34 (21), 6077 (2018).

⁹⁶ G. Keresztury, S. Holly, G. Besenyei, J. Varga, A. Y. Wang, and J. R. Durig, Spectrochim. Acta, Part A **49** (13-14), 2007 (1993).